Journal of Physics: Condensed Matter

Atomistic origin of nano-silver paracrystalline structure: molecular dynamics and x-ray diffraction studies

OPEN ACCESS
IOP Publishing
Journal of Physics: Condensed Matter
J. Phys.: Condens. Matter **34** (2022) 375401 (14pp)
https://doi.org/10.1088/1361-648X/ac7d84

Atomistic origin of nano-silver paracrystalline structure: molecular dynamics and x-ray diffraction studies

Karolina Jurkiewicz[1,2,*], **Michał Kamiński**[3], **Aleksander Bródka**[1,2] and **Andrzej Burian**[1,2]

[1] A. Chełkowski Institute of Physics, University of Silesia in Katowice, 75 Pułku Piechoty 1, 41-500 Chorzów, Poland
[2] Silesian Center for Education and Interdisciplinary Research, 75 Pułku Piechoty 1a, 41-500 Chorzów, Poland
[3] Deutsches Elektronen-Synchrotron, Photon Science, Notkestraße 85, D-22607 Hamburg, Germany

E-mail: karolina.jurkiewicz@us.edu.pl

Received 11 April 2022, revised 2 June 2022
Accepted for publication 30 June 2022
Published 14 July 2022

Abstract

Classical molecular dynamics (MD) and x-ray diffraction (XRD) have been used to establish the origin of the paracrystalline structure of silver nanoparticles at the atomic scale. Models based on the face-centred cubic structure have been computer generated and their atomic arrangements have been optimized by the MD with the embedded-atom model (EAM) potential and its modified version (MEAM). The simulation results are compared with the experimental XRD data in reciprocal and real spaces, i.e. the structure factor and the pair distribution function. The applied approach returns the structural models, defined by the Cartesian coordinates of the constituent atoms. It has been found that most of the structural features of Ag nanoparticles are better reproduced by the MEAM. The presence of vacancy defects in the structure of the Ag nanoparticles has been considered and the average concentration of vacancies is estimated to be 3 at.%. The average nearest-neighbour Ag–Ag distances and the coordination numbers are determined and compared with the values predicted for the bulk Ag, demonstrating a different degree of structural disorder on the surface and in the core, compared to the bulk crystalline counterpart. It has been shown that the paracrystalline structure of the Ag nanoparticles has origin in the surface disorder and the disorder generated by the presence of the vacancy defects. Both sources lead to network distortion that propagates proportionally to the square root of the interatomic distances.

Supplementary material for this article is available online

Keywords: atomic structure, silver nanoparticles, x-ray diffraction, molecular dynamics simulations, embedded and modified embedded-atom methods

(Some figures may appear in colour only in the online journal)

* Author to whom any correspondence should be addressed.

1. Introduction

Silver nanoparticles (Ag NPs) have attracted the attention of many laboratories and industries due to their unique antibacterial [1], catalytic [2], optical [3] and plasmonic [4] properties. The superior features of NPs, compared with their macroscale counterparts, can be attributed to, among others, the increased external surface and the presence of structural defects [5, 6]. However, many structure-property correlations for the metallic NPs have not yet been determined, and the unique phenomena observed for them at the nanoscale, such as enhanced catalytic activity in multimetallic systems [7–9], surface-enhanced Raman scattering behaviour [10] or welding in dispersion [11], are still waiting for a detailed explanation. Critical to further design and optimization of the metallic NPs are appropriate modelling methodologies capable of predicting the structure of NPs at the atomic level, accurately reflecting the morphology and arrangement of atoms for real material.

In recent years, there has been great progress in the development of computer simulation algorithms for structural optimization of the metallic NPs due to the increase in computing power. One of the most fundamental tools to carry out structural optimization on nanoclusters is the first principles calculation according to quantum mechanical theory such as density functional theory (DFT) [12, 13], but this method is limited to a very small systems, usually composed of less than ∼500 atoms. Therefore, it is currently being superseded by other approaches allowing investigation of bigger systems. It is worth mentioning about very recent cluster-mining approach [14] that is based on the generation of a large number of candidate structure models using many constraints and datasets, and then refinement against experimental pair distribution functions [15, 16]. Another class of methods in application to the geometry optimization of NPs is genetic algorithms, which use principles of natural evolution to make a search in the configuration space and look for the most stable configuration of atoms with minimum total energy [17, 18]. Monte Carlo technique and simulated annealing are examples of other 'search' procedures. Monte Carlo method uses the random walk concept [19], whereas the simulated annealing tries to find the global minimum [20]. Besides, classical molecular dynamics (MD) simulations can be applied to study large NPs with a size much greater than ∼1000 atoms. MD and other approaches numerically solving Newton's equations of motion require the use of semi-empirical atomistic potentials, which enable calculations of the total energy and interatomic forces. Early atomistic simulations employed pair potentials, usually of the Lennard-Jones or Morse type [21, 22], but they give only qualitative agreement with the experimental data. A few decades later, Daw and Baskes [23] and Finnis and Sinclair [24] proposed a more advanced potential form called the embedded atom method (EAM). In contrast to the previously mentioned pair potentials, EAM incorporates many-body interactions between atoms, which are responsible for a significant part of bonding in metals. Later on, a modified version of EAM, i.e. modified embedded atom method (MEAM) has been developed [25]. The EAM and MEAM potentials are broadly used in the majority of simulations of metals and metallic alloys and they exhibit a high degree of compliance with experimentally observed phenomena e.g. elastic [26] and thermal properties [27] or energy of defects [28, 29]. In 2000 and 2003 this MEAM formalism has been extended, including consideration of the second nearest-neighbour interactions as reported in [30, 31].

Despite a number of studies, the experimental investigations do not give a clear consensus for the atomic-scale structure of the Ag NPs in a large range of sizes. Different symmetries: face-centred cubic (fcc), icosahedral, decahedral, and octahedral were observed, depending essentially on the route of fabrication applied and the size of the NPs [32–34]. On the other hand, recent theoretical findings suggested the preference for decahedral and octahedral symmetry in the Ag NPs [20]. In addition to these reports, the preparation of the spherical Ag NPs has been developed [35–37].

However, throughout many experimental premises [38–41], structural defects are rarely considered by theoretical models. Hence, the models must be refined and a combination of theory and experiment is required to better understand the complex structure of the metallic NPs. The numerical programs, such as *DISCUS* [42] or *DEBUSSY* [43], have been developed to generate structural models and to compute powder diffraction patterns for nanocrystalline, defective and/or non-periodic systems including a large variety of disorder problems. As an alternative to traditional line profile analysis techniques for nanomaterials (for example the Rietveld or Warren-Averbach methods), the reciprocal-space Whole Powder Pattern Modelling method has been proposed to study nanocrystalline atomic clusters with various lognormal size distributions [44–46].

In this paper, an alternative method that uses MD with the EAM- and latest MEAM-type potentials to optimize the energy of generated structural models containing structural defects and then to calculate structure factors and pair distribution functions is proposed. The energy minimization of the models is a great advantage of this approach over models generated in programs such as *DISCUS* or *DEBUSSY*, which may provide non-equilibrium atomic configurations. Another advancement of the herein used method is the fact that the results obtained from MD simulations are compared with the experimental data, in both reciprocal and real spaces, not just in one space, as is usually done in commercial packages. The only good compliance between the experimental and model-based data in both spaces is treated as a measure of the model reliability, allowing resolving of the local and long-range structure with equally important weight. It is worth mentioning that such an approach goes beyond the standard crystallography methods, which fail in the case of nanomaterials due to the finite size effects and possible structural defects leading to deviations of atoms from positions in bulk crystalline counterparts. Information about short-range atomic order and defects is not contained in the Bragg peaks, but in

a diffuse background. Total scattering methods such as the Debye equation [47] and the atomic pair distribution function analysis recover the Bragg peaks and diffuse scattering, and extract important structural information about local atomic packing and disorder. Most of commercial packages for the simulations of powder diffraction patterns, e.g. *MERCURY* [48], assume the periodicity of the atomic arrangement and use only the Bragg peaks to generate the model of structure. In the presented approach no assumption on the atomic periodicity is taken and the diffraction patterns are calculated with the use of the Debye scattering equation.

The obtained structural information is important to understand the underlying mechanisms controlling e.g. the catalytic properties of nanosized metals. The knowledge of the catalytic reaction mechanisms will be improved if we can relate the catalytic activity to the structural aspects of the materials because most of the catalytic reactions are structure sensitive, and hence, methods to get more insights into structural aspects are highly needed [49]. The problem of the mechanism of the catalytic activity occurring at the surface of a solid catalyst has been studied since decades [50]. It has been shown that increased catalytic activity of various NPs is associated with undercoordination of atoms and the presence of defect sites on the surface. The high catalytic activity at these sites is a consequence of the formation of maxima in the surface electrostatic potential [51]. Such a tendency has been also observed for other nanosized particles [52–54]. Recently, it was shown that both structurally-ordered and structurally-disordered NPs can reach high catalytic activity, but by different mechanisms [55]. The structurally-ordered catalysts feature homogenously strained lattice parameters. In contrast, the structurally-disordered catalysts own their high activity to the high degree of surface defects. The debate whether surface or bulk atomic arrangement has a bigger impact on the catalytic activity is fuelled by the lack of techniques that are available to measure and quantify structural order/disorder in the near-surface layers, thereby preventing the identification of unambiguous relationships between the structure and activity. Therefore, in this article, we demonstrate the method to quantify the atomic arrangement and network distortion of the studied NPs in both the surface and core parts.

2. Experimental details

The Ag NPs were synthesized inside pores of amorphous SiO_2 using the Stöber sol–gel method [56] with $Ag(CH_3COO)$ as the precursor. The size of the NPs in this synthesis method is controlled by the size of pores in the SiO_2 carrier. The final composition and structure are controlled by the reduction process in 773 K for 1 h under hydrogen flow. The entire chemical treatment and reduction procedures as well as the transmission electron microscopy (TEM) investigations were described in details in [57].

The wide-angle x-ray diffraction (XRD) measurements of the Ag NPs were carried out using a laboratory Rigaku Denki D/MAX Rapid II-R diffractometer equipped with a rotating Ag anode, a two-dimensional imaging plate detector and a graphite monochromator. This set-up enables collecting the scattering data in the wide-range of the scattering vector length, $Q = 4\pi \sin(\theta)/\lambda$, up to $Q_{\max} = 20$ Å^{-1}, yielding the atomic pair distribution function of a good resolution; $\lambda = 0.5608$ Å is the wavelength of the incident beam and 2θ is the scattering angle. A detailed description of the XRD experiment and the data reduction and normalization can be found in [57]. In order to correct for the instrumental broadening in the experimental data the (111) peak profile of the NIST SRM 640e Si standard was measured under instrumental conditions identical to those of the sample. During the measurements the temperature in laboratory was kept constant, 293 K.

3. Molecular dynamics simulations and calculations of x-ray scattering data

The quantification of the atomic structure using approaches like the Rietveld refinement and the Scherrer equation is impracticable in the case of the NPs and includes a large error since the NPs are 'crystallographically challenged materials' with deviations from perfect crystallinity [58]. Therefore, the analysis of the total scattering (Bragg and diffuse scattering) and the atomic pair distribution function approach were employed [59, 60] to obtain reliable information about the structure of the investigated Ag NPs. The model-based structure factor and the atomic pair distribution function were computed using the MD simulations. The model of the Ag NPs, defined by ensembles of the Cartesian coordinates of atoms, has been optimized performing the MD simulations with interatomic simulations described by the EAM and MEAM in the *LAMMPS* software [61].

Although NPs can have various morphologies due to different preparation methods, in the present work we discuss the spherical NPs, since the TEM investigations revealed that most of the single Ag clusters have an approximately spherical shape and exhibit a trimodal size distribution that has been published earlier [57]. Accordingly, the name NP is used here for an individual cluster of atoms that is regarded as a single nanocrystal. Therefore, the starting atomic models for the MD simulations were generated assuming spherical nanoclusters of diameters, d, corresponding to the maxima of three Gaussian functions that approximate the distribution (55, 115 and 470 Å). All atoms in the created clusters of the three different sizes were arranged in the fcc structure with the lattice parameter $a = 4.086$ Å, reported for bulk Ag at room temperature [62]. The numbers of atoms contained in the models of the NPs, N, and their weights, w, are collected in table 1. It should be noted that the weights taken for the calculations were parameters adjusted based on the previously optimized paracrystalline model of the structure [57].

The MD simulations were carried out for the canonical ensemble at 300 K, and the equations of motion were integrated using the velocity Verlet algorithm, with a time step of 2 fs. Simulations for each cluster were carried out for a total number of 5×10^5 time steps. The temperature of the system

Table 1. Parameters for the Ag NPs used in MD simulations: the diameters of spherical particles, d, the numbers of atoms in NPs, N, and their percentage weights, w.

d (Å)	55	115	470
N	5089	46 553	3179 491
w (%)	33	65	2

was stabilized using the Nosé-Hoover thermostat with the temperature damping parameter of 100-time steps. No drift of the total energy with time was observed, what was checked by simulations in microcanonical ensemble. It must be stressed that the applied thermostat account well for the influence of the thermal motions of atoms, i.e. the MD simulations generate the thermal disorder as it was demonstrated in [63] for the Au NP. Therefore, the results of simulations can be directly compared with the experimental intensity data measured at room temperature. The coherent powder intensity per one atom for NPs is expressed by the so-called Debye equation:

$$I_{\mathrm{coh}}(Q) = \frac{1}{N} f^2(Q) \sum_{i=1}^{N} \sum_{j=1}^{N} \frac{\sin(Qr_{ij})}{Qr_{ij}} \tag{1}$$

where r_{ij} means the distance between ith and jth atoms. The application of the Debye equation to this type of calculations is detailed by Gelisio and Scardi [47].

The diffraction data for non-crystalline materials are usually represented by the structure factor, defined as follows:

$$S(Q) = \frac{I_{\mathrm{coh}}(Q)}{f^2(Q)} \tag{2}$$

where $I_{\mathrm{coh}}(Q)$ is derived from the measured x-ray intensity corrected and normalized to electron units and $f(Q)$ is the atomic scattering factor of Ag [64]. Final positions of atoms in clusters, obtained from the MD simulations, were used to calculate the normalized scattering intensity function per one atom, and then the structure factor can be obtained according to [65] as:

$$S(Q) = 1 + \frac{1}{N} \left[\sum_{i=1}^{N} \sum_{j=1}^{N} \frac{\sin(Qr_{ij})}{Qr_{ij}} \right]_{i \neq j}. \tag{3}$$

The unwanted small-angle component of the intensity calculated from the Debye equation can be eliminated using procedures described in [65–67].

In order to validate those calculations, the $S(Q)$ for cluster of 5089 atoms was also averaged over ten configurations at different time steps after energy stabilization and results are almost the same as those obtained for the final configuration after 5×10^5 time steps (see figure S8 in supplementary material). It means that averaging over the ensemble was equivalent to the time averaging and such obtained atomic configurations can be used to generate the structural models of the Ag clusters. The $S(Q)$ derived from the total intensity measured in the experiment, according to equation (2), can be directly compared with the theoretical $S(Q)$ calculated according to equation (3). The experimental structure factor contains contributions from scattering by the Ag NPs of different sizes, as revealed by the TEM images. In order to take into account the wide size distribution of the studied NPs, the total theoretical structure factor was computed as a weighted average over the individual structure factors for three clusters of different d, with the weights w collected in table 1. In such calculations it is assumed that the individual clusters scatter independently. The w values were estimated in our previous paper [57] using the paracrystalline model reconstructing all features of the experimental total scattering data.

In the next step, the $S(Q)$, both experimental and theoretical, were converted to the real space representation in the form of the pair distribution function, $G(r)$, by the sine Fourier transform as follows:

$$G(r) = 4\pi r[\rho(r) - \rho_0] = \frac{2}{\pi} \int_0^{Q_{\max}} Q[S(Q) - 1] \sin(Qr)\, dQ \tag{4}$$

where $Q_{\max}$ is the upper value of Q achieved in the measurements. The function $4\pi r^2 \rho(r)\, dr$ determines the number of atoms within the spherical shell of the radius r and the thickness dr, and ρ_0 is the number density. Thus, the $G(r)$ function provides information about the distribution of interatomic distances in the average atomic cluster of the investigated material. The first peak of $G(r)$ corresponds to the nearest-neighbour distance, and the subsequent peaks are related to second-, third- and next-neighbour coordination spheres. The $G(r)$ is more sensitive to the local deviations from the structural periodicity than $S(Q)$, while $S(Q)$ is better suited for the analysis of longer-range interatomic correlations. Therefore, in order to find models of the Ag NPs reproducing both their nearest-neighbour and longer-range structure, the results of the model-based simulations were compared with the experimental data both in reciprocal and real spaces.

According to [68, 69] the effect of the instrumental broadening can be described by convolution of the pure diffraction intensity $I(Q)$ with the apparatus function $I_{\mathrm{i}}(Q)$ giving the measured intensity function $I_{\mathrm{m}}(Q)$:

$$I_{\mathrm{m}}(Q) = I(Q) * I_{\mathrm{i}}(Q) = \int_{-\infty}^{\infty} I(Q') I_{\mathrm{i}}(Q - Q')\, dQ'. \tag{5}$$

This instrumental effect can be accounted for by convoluting the model-based intensity with the instrumental function, and that method is applied here. In an alternative approach the measured intensity $I_{\mathrm{m}}(Q)$ and instrumental one $I_{\mathrm{i}}(Q)$ can be used to obtain the pure diffraction intensity $I(Q)$ solving equation (5) and the results obtained are shown in Supporting Information (see figures S3–S7 in supplementary material).

4. Results and discussion

In the first step, the results of MD simulations using the EAM for the defect-free fcc model were analysed. In such a case,

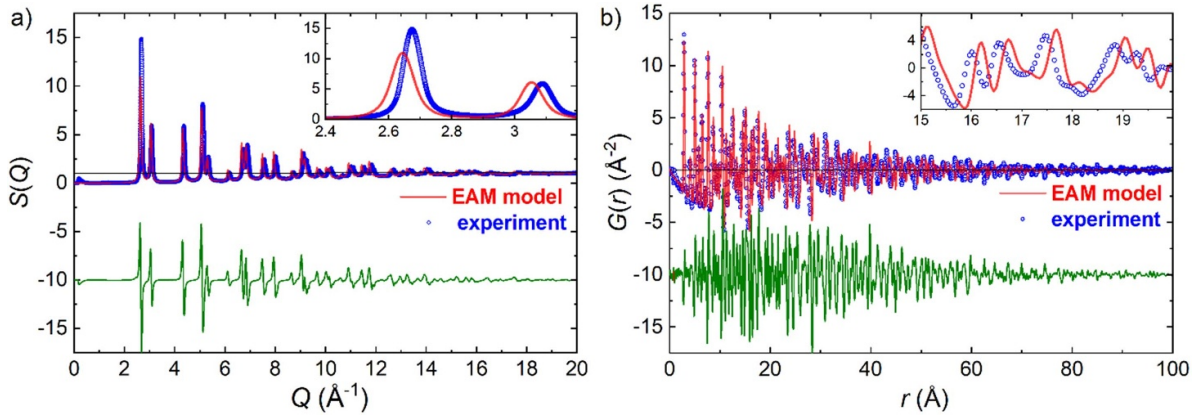

Figure 1. The experimental structure factor (a) and the pair distribution function (b) for the Ag NPs and their counterparts obtained from the MD simulation using the EAM potential for the defect-free models. The differences between the theoretical and experimental functions, plotted in green, are shifted for clarity. The insets show zooms on selected data ranges.

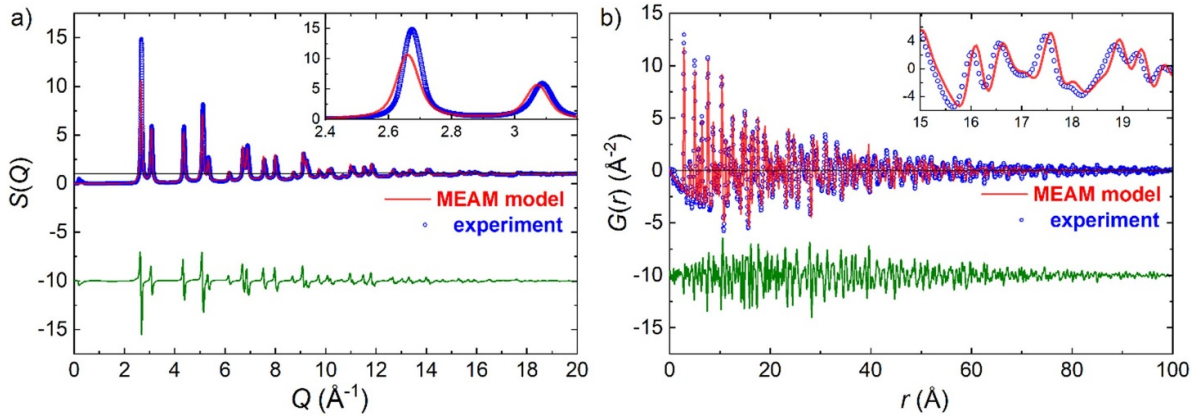

Figure 2. The same as in figure 1, but the theoretical results are obtained for the MEAM potential.

the nanosize effect is principally the main factor determining the observed diffraction peak broadening. Also, the position of the peaks, determined by the interatomic distances may differ from those observed for bulk Ag counterparts. The undercoordination of the surface atoms leads to the lattice deformation and possible modification of the interplanar distances. Moreover, the atomic disorder causes the damping of peaks. Figure 1 presents the comparison of the structure factor and the pair distribution function obtained from the MD simulations with the experimental functions. As can be seen, the experimental $S(Q)$ shows well-defined diffraction peaks, which are broadened relative to those of crystalline material having long-range ordering. Experimental $G(r)$ is rich in structural features, but they are attenuated almost to zero at interatomic distances of around 100 Å. One can see that the amplitudes of the simulated $S(Q)$ and $G(r)$, and their damping with increasing values of Q and r, respectively, quite nicely reconstruct the experimental results, which indicates good approximation of the NP's size distribution. The goodness the model-based simulations can be visualized by viewing the experimental and calculated functions together with discrepancies between them, as suggested in [70].

The major discrepancies of the theoretical and experimental functions are observed in the peak positions, both of $S(Q)$ and $G(r)$ (see the insets in figure 1). The reason for that may be twofold: the applied EAM potential does not describe the interatomic separations precisely or the starting model is incorrect. In order to dispel these doubts and evaluate the performance of EAM simulations, the geometry of the same Ag nanoclusters was optimized using the MEAM potential.

The structure factor and pair distribution function obtained from MD simulations for MEAM potential are presented in figure 2. It is visible that this potential leads to better results than the EAM. Particularly, the MEAM better reconstructs the interatomic distances than the EAM. The peaks of theoretical diffraction data, calculated based on the model using the MEAM potential, shift towards the positions of experimental peaks. In other words, the Ag NPs model optimized using the MEAM better suits the experimental data. Interestingly, in our recent paper on MD simulations of the Au NPs the experimental spatial correlations between atoms were clearly better described by the EAM potential when compared with that of MEAM [63]. The literature report for NiTi alloys showed the higher accuracy of the lattice constant by employing MEAM

potential [71]. In turn, the EAM better described the recrystallization of NiTi at high temperatures. Also for liquid Ni, the critical comparison of these two potentials revealed that the MEAM can give a representative picture of its structure factors and other properties [72]. Thus, the above-mentioned facts testify that the performance and accuracy of the potentials used in the MD simulations of metals strongly depend on a system and studied properties. Nevertheless, it is worth noting that the embedded atom methods provide better reliability of lattice parameters and surface characteristics than tight-binding methods [73] and in the case of the small Au NPs generates optimized structures very similar to those obtained from *ab initio* DFT calculations [74]. It is worth noting that literature data have reported that the agreement of the simulation results based on EAM or MEAM with respect to the experimental data or DFT calculations varies, depending on the system and property that is studied. One can give as an example simulations for Pt NPs where the MEAM resulted in slightly closer values of lattice and stiffness constants to experimental data than the EAM. In turn, an analysis of the stability of Pt clusters revealed that MEAM potentials failed while EAM manage to reproduce the structural integrity of NPs that can be synthesized and remain stable at room conditions in experimental conditions [75]. Another example is the investigation of the generalized stacking fault energy for models of Al, Ni and Cu metals. It was found that the EAM potentials for Al and Cu, whereas MEAM for Ni, predict better the effect of vacancy defects on the stacking fault energy in regards to DFT calculations [28]. Furthermore, the paper of Chen *et al* clearly compares the performance of EAM and MEAM potentials in predicting the plasticity and fracture behaviors of hcp metals. Depending on the element, Mg, Co, Ti, and the property under probe, the errors between the DFT and EAM or MEAM results vary significantly [76]. Also, for bimetallic case of Co–Pt nanoclasters it was reported that EAM and MEAM potentials give different results, depending on the tested property [77]. MEAM potential gave a better prediction of the order-disorder transition temperature, whereas lattice parameters were better predicted by the EAM. Results of these investigations indicate the sensitivity of the studied properties on the potential model.

Despite the fact that the model of the average atomic structure of the Ag NPs optimized with the MEAM showed good agreement with the experimental data, some discrepancies in the peak positions and amplitudes, compared with the measured ones, can still be observed. The peaks of the simulated $S(Q)$ are shifted towards lower Q and, consequently, the maxima of the model $G(r)$ move towards longer interatomic distances that can be especially seen for the high-r range (see inset in figure 2(b)). Therefore, when one assumes the MEAM correctly describes the interatomic interactions and distances in small Ag clusters, there must be an additional source of the observed differences in the $S(Q)$ and $G(r)$ peak positions. As the dynamic disorder is generated by the thermal motions of atoms, one can suspect that the static disorder is the source of the observed discrepancies between the experiment and model. Recently, it has been shown that defective structures, i.e. showing local symmetry loss, missing atoms, dislocations, or extended lattice imperfections, may be preferred over perfectly regular ones in the Ag NPs [78]. The non-symmetrically grown or defective clusters were found to be more stable than highly symmetric ones in terms of their surface energy.

Noble metal NPs are prone to stacking faults and this type of defects is the most often considered in the literature for the explanation of the lattice distortion [6]. Contrary, many previous papers suggested the presence of defects in the form of vacancies in the metallic NPs [29, 79–82]. The presence of vacancy defects in metallic NPs is rather a controversial hypothesis, and the number of possible vacancies is difficult to estimate experimentally. Therefore, in this article the hypothesis on the presence of vacancies in Ag NPs has been verified and in the next step, the model of Ag clusters containing vacancies was considered. Several studies have tried to estimate the concentration of vacancies in NPs by extrapolating empirical relationships established for the formation energy of bulk vacancies down to the nanometer scale [29, 82, 83]. However, no consensus has been reached. Therefore, the number of vacancies in the Ag models generated here was adjusted based on the best agreement of model-based $S(Q)$ and $G(r)$ with the experimental data. The location of defects in metallic NPs cannot be unambiguously established. Consequently, the vacancies were created by the removal of randomly chosen atoms in each cluster. That means both surface shells and the core of the NPs may contain vacancies. The produced Ag clusters with different vacancy concentrations in the range of $1-5$ at.%, were then relaxed performing the MD simulations. We assumed an accuracy for the determination of the vacancy concentration as 1 at.%. The best correspondence with the measured $S(Q)$ and $G(r)$ has been obtained for the MEAM with 3 at.% of vacancies. For the concentration of 1 and 5 at.%, the agreement of calculated structure factors and pair distribution functions with the experimental data was clearly worse. It is worth adding that he presence of the Schottky defects in noble metal nanoclusters was also investigated using the kinetic Monte Carlo approach and the vacancy concentration in the range of $3-5$ at.% was estimated [84], which is in line with the values obtained herein.

The influence of the vacancies on the diffraction data can be seen by comparing the results presented in figures 3 and 4 with those in figures 1 and 2, respectively. The first effect that one can observe is the stronger damping of model-based data. The second consequence of the presence of vacancies is the shift of diffraction peaks towards the experimental ones that is especially visible for the MEAM model. Both effects reduce the difference between the simulated and experimental data. The better compatibility of the model is particularly seen for medium and long interatomic distances (see the inset in figure 4(b)). The positions of $G(r)$ peaks agree very well in this range, whereas peaks for the model without defects are shifted towards longer distances. Also, in the case of the EAM potential, the model with vacancies slightly improves the agreement with the experimental data (see figure 3), however, the improvement is unsatisfactory.

From the performed modelling, one can suggest that there are two sources of the static disorder in the Ag NPs: (a) the

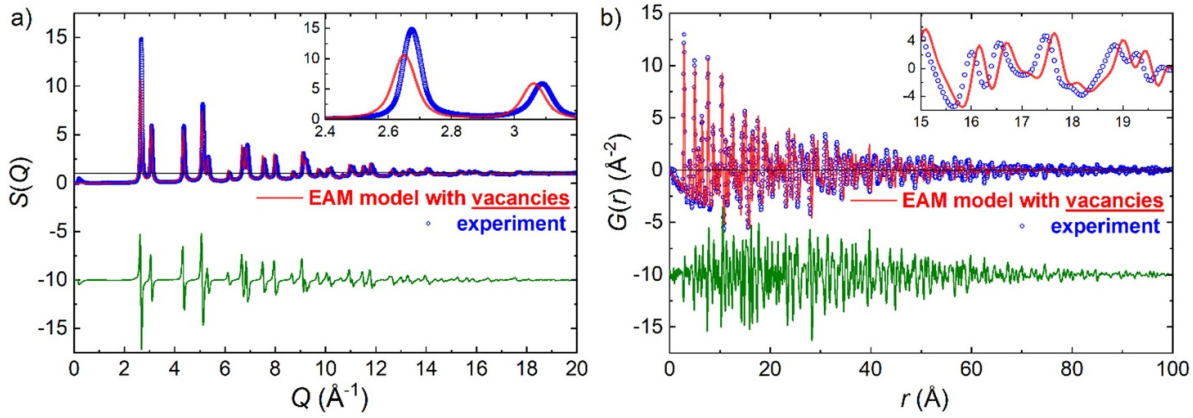

Figure 3. The same as in figure 1, but for NPs with 3 at.% of vacancies.

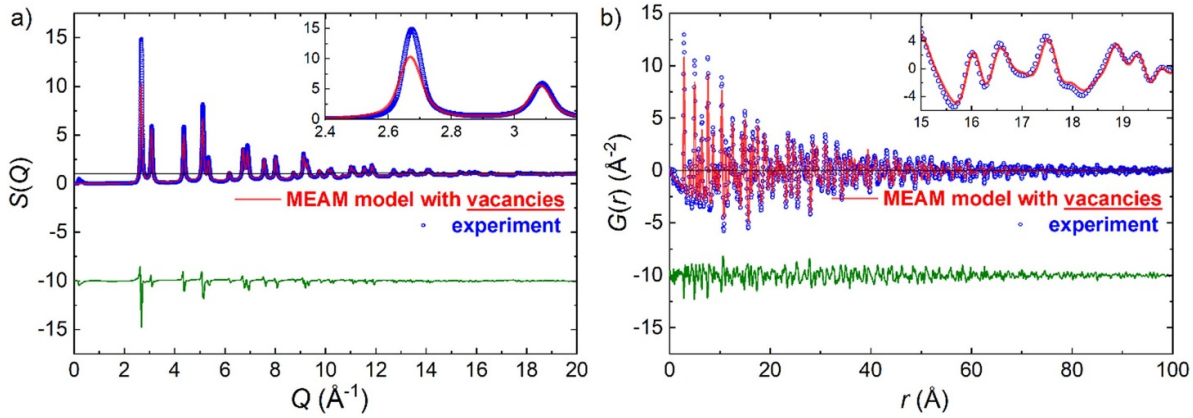

Figure 4. The same as in figure 2, but for NPs with 3 at.% of vacancies.

network distortion induced by the finite size of the NPs and under-coordinated atoms on the NP surface and (b) the structure deformation generated by the vacancy defects. The quantified characterization of the static disorder may be done by the analysis of the distributions of the interatomic distances and coordination numbers in the modelled clusters, without and with vacancies, for core and surface atoms. The surface layer was defined as a spherical shell on the cluster surface with a thickness of 3.5 Å, and the core layer was the sphere in the centre of the particle with a radius of 10 Å. The determined distributions are shown in figures 5 and 6. One can see that the width of the nearest-neighbour interatomic distance distribution is independent of the cluster size. There is almost no difference in this distribution for 55 and 470 Å. However, there is a clear dependency of the width of the histograms for the nearest-neighbour distances on the location of atoms in the clusters. The distributions are wider for the surface shell than for the core, independent of the presence or lack of vacancy defects. The mean values of the nearest-neighbour distances for atoms lying in the surface shell are slightly shorter than those for the core atoms. For the smallest clusters, the difference in these values is the biggest due to the higher proportion of the number of the surface atoms to the total number of atoms. Additionally, the standard deviations of the mean values of the nearest-neighbour distances are bigger for the surface shell than for the core part. Due to the differences between the surface and core interatomic distances, it is difficult to give one precise value of the lattice parameter for the studied Ag NPs. Moreover, one can see that for smaller clusters, the values of both surface and shell nearest-neighbour Ag–Ag distances are shorter than for the bigger particles. This is true for both models with and without vacancies. For the model without vacancies, the lattice distortion is due to surface relaxation. The mean value of the nearest-neighbour distance for the core of the Ag clusters studied here is in the range 2.88−2.91 Å, which agrees well with the experimental value of 2.89 Å for bulk Ag [62]. Thus, in the case of real nanomaterials composed of a wide distribution of the defective NPs of different sizes, the inter-atomic distances may exhibit a wide distribution depending on the NP's size and the distance from the NP's core. Consequently, the associated properties of the surface and core regions may be very distinct. It is worth noting that the plots presented in supplementary material in figures S3–S6 show very similar agreement of the model-based simulations with the experimental data when compared with those displayed above. It means that both approaches to the instrumental broadening problems lead to similar conclusions about the proposed structural models.

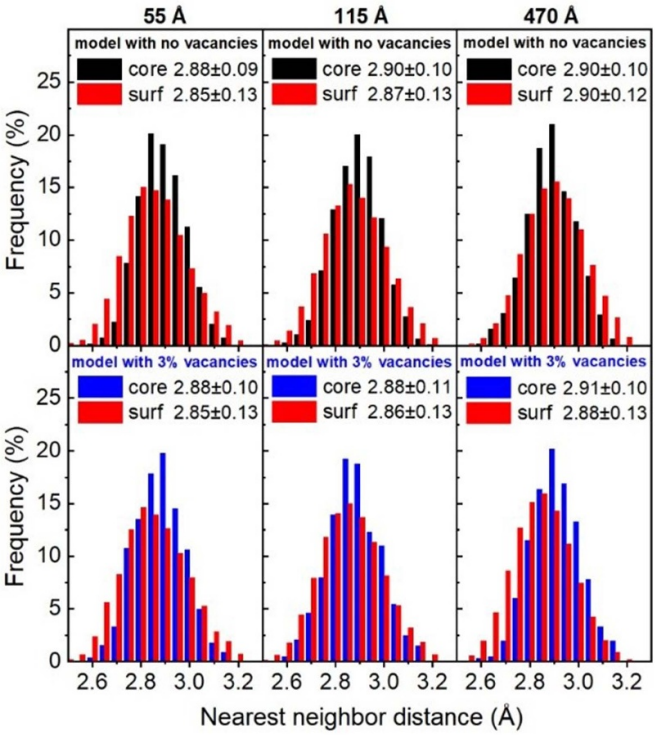

Figure 5. Distributions of nearest-neighbour interatomic distance obtained from the MEAM simulations for atoms from the core and surface layers of NPs with the diameters indicated. The top panels concern the NPs without point defects, while the bottom panels concern the NPs with vacancy defects. The average nearest-neighbour distances, together with their standard deviations, are given on the panels.

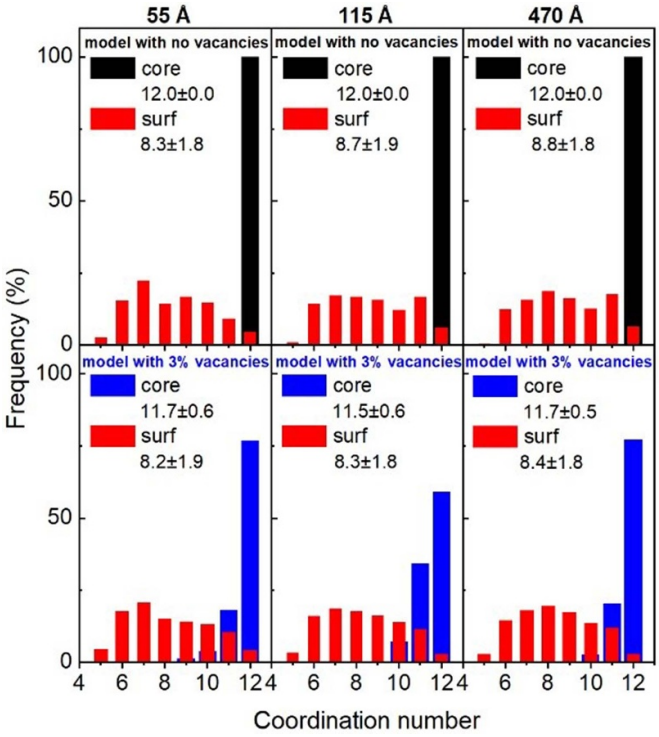

Figure 6. As in figure 5, but for the coordination numbers.

Literature on the size-dependent structure of NPs is abundant, and it is known that surface relaxation may cause contraction or expansion of the unit cell parameters on the surface and average lattice constants, depending on the specific material [85–89]. Studies on most fcc metal NPs, such as Ag, Au and Pt [57, 90], point out a shrinkage of the cell parameter when the size of NPs decreases. However, there are a few exceptions—e.g. Ni tends to expand with smaller size [91]. Analysing the case of the Ag NPs, one can see that the effect of the surface relaxation and lattice parameter's behaviour depends on the synthesis conditions and treatment, like whether the NPs are free or embedded in a matrix [92–94]. Moreover, it is possible to produce the Ag NPs of diverse shapes [95, 96], and the shape is another important parameter controlling the surface relaxation. It was found that the particle shape can lead to around 10% of the total lattice variation [97]. It is therefore difficult to predict the structural properties of the whole family of the Ag NPs. The model proposed in this work relates to a specific case of spherical NPs produced by the sol–gel method inside SiO_2 matrix. However, the simulation procedure and structure refinement approach may be applied to any other type of NPs.

To assess more details of the atomic-scale structure models for the Ag nanoclusters, the distributions of the nearest-neighbour coordination numbers (see figure 6) were analysed. For all core regions in clusters without vacancies the first Ag–Ag coordination number is strictly 12, as in bulk Ag of the fcc-type densely packed structure. In turn, in the surface shell of the studied clusters, atoms are undercoordinated and the first coordination number shows a distribution from around 5–12 with an average value of around 8–9, while the average value increases with the cluster size. This observation is reasonable because the fraction of the surface atoms diminishes with increasing cluster diameter. Similar behaviour was observed based on the experimental and theoretical diffraction data for various metal NPs [63, 84, 98, 99].

It should be noted that the undercoordinated atoms at NP surfaces experience significant relaxation while the core atoms are largely not affected by the surface-related effects. Therefore, these two types of atoms may not exhibit the same structural patterns. For models with vacancy defects, the population of atoms with high coordination numbers decreases while more atoms exhibit lower coordination numbers. The average first coordination number for models with vacancies decreases by around 0.1−0.5 compared to neat clusters. However, the trend in the coordination number values with the cluster size is maintained. The decrease of the cluster size leads to diminishing the coordination number for atoms on the surface shell.

The resultant structural model refined by MEAM method for 5.5 nm Ag cluster with vacancy defects is presented in figure 7(a). One can see the effect of the thermal and static network distortion generated by the MD simulations. The positions of atoms show displacements from the crystal planes. Atoms in the inner part of the NPs show displacements smaller than atoms located closer to the NP surface. The studied Ag NPs do not exhibit a core–shell structure with a clearly demarcated border between these two zones, but

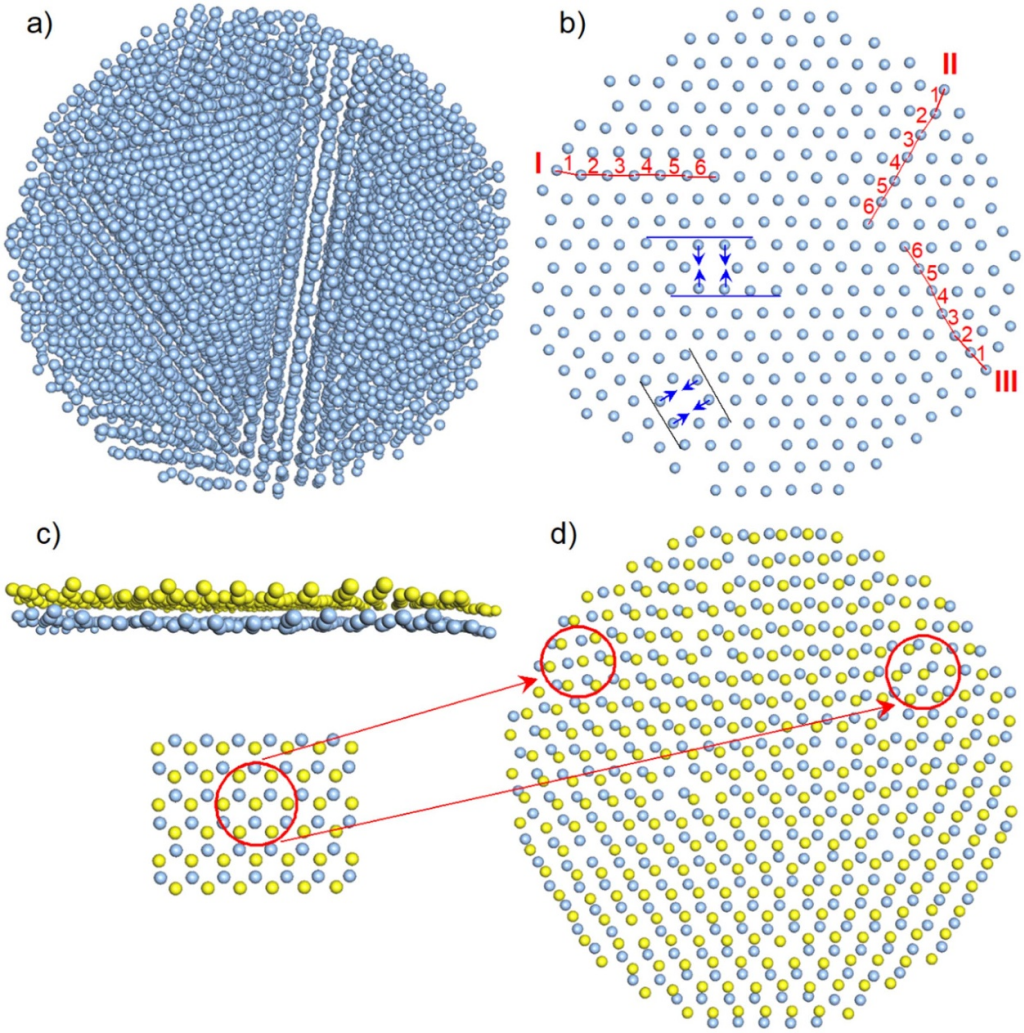

Figure 7. (a) Model of Ag NP with diameter of 55 Å and 3 at.% concentration of vacancy defects. (b) Central atomic layer cut from the model. The lines I, II and III with marked interatomic distances 1−6 show the propagation of the paracrystalline distortion from the surface to the core, the values of the distances are given in table 2. (c) Two central atomic layers with a deviation from planarity on edges. (d) The planar projection of two central atomic layers. The red circles highlight the distortion from the close-packing of atoms. The model on the left shows the perfect fcc structure with hexagonal close-packing.

rather the disorder gradually disappears into the inner layers. Figure 7(b) demonstrates an example of the close-packed atomic plane extracted from the equator part of the model shown in figure 7(a). The guide red curves marked as I, II and III present the atomic disorder and the change in the nearest-neighbour interatomic distance going from the surface towards the core (numbers from 1 to 6). The values of the nearest-neighbour Ag–Ag distances in the I−III curves are presented in table 2. The interatomic distances in the surface shell, marked with number 1, are clearly shorter than the distances located more in the inner part of the cluster, marked with the number 6. However, the increase in the interatomic distance from the surface to the core is not monotonic.

The removal of atoms in the network (creation of vacancy defects) leads to local rearrangement of atoms and network distortion around the defects. This is illustrated in figure 7(b) using the guide blue lines showing the course of ideal atomic layers. Atoms around the vacancy defect shift from these lines toward the missing atom (see the blue arrows in figure 7(b)). The presence of vacancies in the core part of the NPs is consistent with previous predictions of a possible arrangement of vacancies in Ag nanoclusters by Taherkhani *et al* [100]. They established that the most stable position of the vacancy defect is at low-coordinated surface sites while surprisingly, the next favourable position is at core sites, which can better

Table 2. Nearest-neighbour distances between Ag atoms marked with numbers 1−6 in figure 7(b), showing the network distortion from the surface to the core part of the NPs.

	Nearest-neighbour interatomic distance (Å)					
Line number	1	2	3	4	5	6
I	2.63	2.83	2.90	2.86	2.90	2.96
II	2.83	2.84	2.88	2.93	2.75	2.96
III	2.77	2.81	2.92	2.91	2.86	2.98

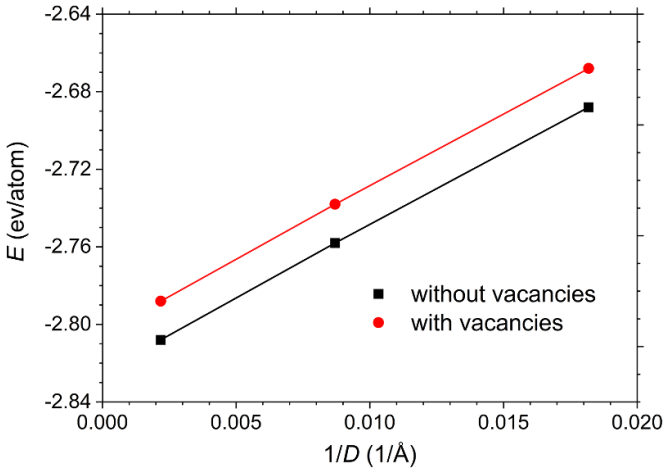

Figure 8. The potential energy per atom as a function of the inverse of the NP diameter. The lines are fits to the simulation data.

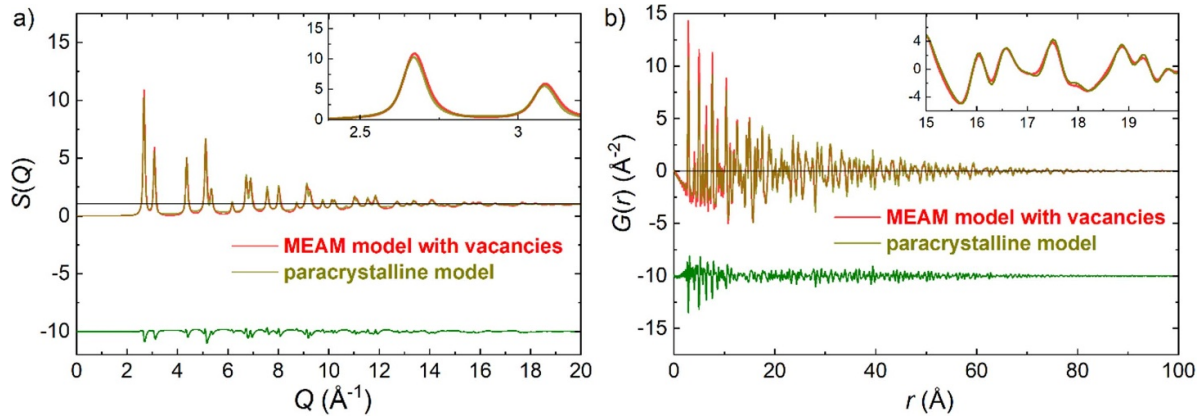

Figure 9. Comparison of the structure factor (a) and pair distribution function (b) calculated for the MEAM model of Ag NPs containing 3 at.% of vacancies with those derived based on the paracrystalline model. The differences between both model functions, plotted in green, are shifted for clarity. The insets show zooms on selected data ranges.

accommodate strain with respect to vacancies on higher-coordinated surfaces. Lower coordination numbers introduced by vacancy defect are responsible for slight increase of the potential energy as presented in figure 8. The values of the energy per atom for the optimized NP's models were derived for the final MD configurations. As can be seen, the energy increases when the size of the NPs decreases similarly as for the gold NPs [63].

Figure 7(c) shows two adjacent layers cut from the equatorial part of the model from figure 7(a). As a result of the presence of point defects and atomic disorder on the surface, the layers are not ideally planar. They exhibit a deviation from planarity on edges. In figure 7(d), a flat projection of the two central layers is presented. The red circles highlight the regions with a clear displacement of atoms from ideal positions of the close-packing. The arrangement of atoms inside the red circles in figure 7(d) loses their periodic order compared to positions shown for the fragment of the perfect fcc structure with hexagonal close-packing (on the left).

In our previous article on the atomic structure of various silica-supported metal NPs, we demonstrated that they exhibit the fcc-type structure with paracrystalline distortion [57]. The paracrystalline disorder, in the form of the standard deviation of the inter-atomic distances, propagates proportionally to the square root of the distance and correlates with the size of the NPs [69, 101]. In figure 9 we compare the diffraction data computed based on the paracrystalline model for Ag NPs with the results obtained from the MD simulations. The agreement between both sets of theoretical data is very good both in $S(Q)$ and $G(r)$. The MD model of Ag nanoclusters with vacancy defects reflects the local distortion of the atomic network generated by the paracrystalline disorder. The positions of the interatomic distances within the first $G(r)$ peaks are well reconstructed by these models. Moreover, the inset of figure 8(b) shows that both approaches are able to describe correctly longer interatomic distances. Therefore, the MD model containing point defects may be treated as a physical realization of the theoretically predicted paracrystalline structure of metal NPs.

Nowadays there is great interest in dual atom/hybrid NPs involving metals, e.g. metal-organic frameworks (MOFs), for applications such as catalysis, gas storage, pollutants purification, electrochemical cells, and drug delivery [102]. The principal challenge in the group of MD-based simulations

is to employ an accurate and computationally efficient potential of interactions for all elements. The EAM needs seven functions to describe a binary alloy. These are embedded functions and electron density for every type of atoms and three functions of pair interactions. The form of electron density function is crucial for this method. In the EAM the electron density is spherically symmetric and the same is for all atoms in the system. Therefore, EAM cannot model a matter with different types of bonds, i.e. is inadequate for intermetallic compounds involving strongly covalent elements, as it cannot describe the directional bonding [103]. In turn, the electron density function in MEAM is determined as the sum of components. Each component is responsible for various directions of the bonds. Due to the ability to distinguish between different types of bonding, MEAM can be used to model individual metals, as well as their alloys. Thus, the modelling procedure with MEAM described in this article could also be successfully applied for resolving the structure of metal alloys. The first step would be to construct a start-up model of bimetallic NP with an appropriate size, shape and phase composition. Then, the point defects should be introduced. The final step would be the minimization of the model energy by the MEAM. The classical force field simulations can be also used to study structural properties of MOFs. However, such an approach requires further development to automate accurate force field parameterization. Because of the extreme chemical diversity across thousands of MOF structures, this problem is still mostly unsolved today [104].

5. Conclusions

In this work, two interatomic potentials designed for metals, EAM and MEAM, were examined for the Ag NPs produced by the sol–gel technique on a porous silica template. Using the MD simulations, the ability of these potentials to predict the atomic-scale structure of the Ag NPs was tested. It was shown that the MEAM method better describes the interatomic distances for the Ag NPs of roughly spherical shape and sizes from the trimodal distribution in the range from around 2 nm up to 90 nm. As a result of the MD simulations, the theoretical model of the Ag nanoclusters containing vacancy defects was proposed. It must be mentioned that our previous studies of the structure of Au NPs showed that the application of the EAM potential to model the structure of these NPs gave better agreement with experimental diffraction data than in the case of the MEAM. This proves that the applicability of different potentials described in the literature for the prediction of the atomic arrangement must always be verified by experimental structural data.

The optimized model of the average structure provided detailed information about the arrangement of atoms in the studied silver NPs. It was demonstrated that the model assuming: (a) the weighted average over three spherical clusters with diameters corresponding to the maxima of the trimodal particle diameter distribution from TEM observations (5.5, 11.5 and 47 nm), (b) the fcc arrangement of atoms, and (c) containing 3 at.% of randomly distributed vacancy defects for each cluster reproduces the experimental diffraction data in the form of the structure factor and the atomic pair distribution function very well. The applied approach, taking into account only the most common particle sizes, facilitates the structure modelling in the case of NPs with the multimodal size distribution. This is usually the case for the large-scale production of NPs.

The high ratio of surface atoms to total atoms in the considered nanoclusters produces static disorder reflected in the decrease in the Ag–Ag nearest-neighbour distance and the coordination number in the surface shell. The smaller the size of the cluster, the higher the degree of disorder is observed, and the bigger the discrepancy between the structural parameters of the nanoclusters compared to those reported for bulk Ag. However, such type of network distortion, associated with the finite size of the NPs, does not describe correctly all features of the diffraction data, namely the intensity and positions of peaks. It was nicely presented that including the point defects in the model, in the form of vacancies, introduces additional atomic network deformation, which resembles the paracrystalline distortion, leading to very good agreement of the model-based diffraction data with the experimental results. The separate consideration of the core and surface structural features suggests that the physico-chemical properties of these two regions may be very distinct. The average relative difference of the nearest-neighbour interatomic distances between the surface and the core can be a measure of the lattice strain. Since subtle shifts in the surface arrangement relative to the core lattice have a considerable impact on the catalytic behaviour of metal nanocrystals [105], the development of the synthesis of metal NPs with a high degree of control of the lattice strain, as well as techniques of the strain determination, are important for future research and applications. Here, we presented an effective method for the determination of the mismatch between the surface and the core structure of Ag nanoclusters with various sizes.

The applied procedure of the structure modelling may be used to estimate the concentration of defects in the nanomaterials. Direct microscopic observations of point defects are very demanding and do not provide quantitative data. The XRD measurements may supply structural information that is averaged over a much larger sample volume in comparison with the TEM method. Therefore, computer modelling of the atomic-scale structure and its verification by experimental XRD data is an alternative way to extract information on the average amounts of defects and the degree of disorder in NPs.

Data availability statement

The data generated and/or analysed during the current study are not publicly available for legal/ethical reasons but are available from the corresponding author on reasonable request.

Acknowledgments

K J is thankful for financial support from the Polish National Centre for Research and Development within the LIDER Project (Dec. No. LIDER/24/0131/L-10/18/NCBR/2019).

ORCID iDs

Karolina Jurkiewicz https://orcid.org/0000-0002-4289-7827
Michał Kamiński https://orcid.org/0000-0002-0901-0809
Aleksander Bródka https://orcid.org/0000-0003-1228-8294
Andrzej Burian https://orcid.org/0000-0003-4613-0014

References

[1] Pulit-Prociak J and Banach M 2016 Silver nanoparticles—a material of the future? *Open Chem.* **14** 76–91
[2] Liang M, Su R, Huang R, Qi W, Yu Y, Wang L and He Z 2014 Facile *in situ* synthesis of silver nanoparticles on procyanidin-grafted eggshell membrane and their catalytic properties *ACS Appl. Mater. Interfaces* **6** 4638–49
[3] Stamplecoskie K G and Scaiano J C 2010 Light emitting diode irradiation can control the morphology and optical properties of silver nanoparticles *J. Am. Chem. Soc.* **132** 1825–27
[4] Campos A, Troc N, Cottancin E, Pellarin M, Weissker H-C, Lermé J, Kociak M and Hillenkamp M 2019 Plasmonic quantum size effects in silver nanoparticles are dominated by interfaces and local environments *Nat. Phys.* **15** 275–80
[5] Zhou X, Xu W, Liu G, Panda D and Chen P 2010 Size-dependent catalytic activity and dynamics of gold nanoparticles at the single-molecule level *J. Am. Chem. Soc.* **132** 138–46
[6] Li Z, Fu J-Y, Feng Y, Dong C-K, Liu H and Du X-W 2019 A silver catalyst activated by stacking faults for the hydrogen evolution reaction *Nat. Catal.* **2** 1107–14
[7] Ortalan V, Uzun A, Gates B C and Browning N D 2010 Towards full-structure determination of bimetallic nanoparticles with an aberration-corrected electron microscope *Nat. Nanotechnol.* **5** 843–7
[8] Roy A, Debnath B, Sahoo R, Chandrakumar K R S, Ray C, Jana J and Pal T J 2016 Enhanced catalytic activity of Ag/Rh bimetallic nanomaterial: evidence of an ensemble effect *J. Phys. Chem.* C **120** 5457–67
[9] Wu C H, Liu C, Su D, Xin H L, Fang H T, Eren B, Zhang S, Murray C B and Salmeron M B 2019 Bimetallic synergy in cobalt–palladium nanocatalysts for CO oxidation *Nat. Catal.* **2** 78–85
[10] Zhou L *et al* 2020 Irreversible accumulated SERS behavior of the molecule-linked silver and silver-doped titanium dioxide hybrid system *Nat. Commun.* **11** 1785
[11] Huang Z *et al* 2019 A welding phenomenon of dissimilar nanoparticles in dispersion *Nat. Commun.* **10** 219
[12] Chrétien S, Gordon M S and Metiu H 2004 Binding of propene on small gold clusters and on Au (111): simple rules for binding sites and relative binding energies *J. Chem. Phys.* **121** 3756–66
[13] Kilin D S, Prezhdo O V and Xia Y 2008 Shape-controlled synthesis of silver nanoparticles: *ab initio* study of preferential surface coordination with citric acid *Chem. Phys. Lett.* **458** 113–6
[14] Banerjee S, Liu C-H, Jensen K M Ø, Juhás P, Lee J D, Tofanelli M, Ackerson C J, Murray C B and Billinge S J L 2020 Cluster-mining: an approach for determining core structures of metallic nanoparticles from atomic pair distribution function data *Acta Cryst.* A **76** 24–31
[15] Doan-Nguyen V V T, Kimber S A J, Pontoni D, Reifsnyder Hickey D, Diroll B T, Yang X, Miglierini M, Murray C B and Billinge S J L 2014 Bulk metallic glass-like scattering signal in small metallic nanoparticles *ACS Nano* **8** 6163–70
[16] Banerjee S *et al* 2018 Improved models for metallic nanoparticle cores from atomic pair distribution function (PDF) analysis *J. Phys. Chem.* C **122** 29498–506
[17] Dugan N and Erkoç Ş 2009 Genetic algorithms in application to the geometry optimization of nanoparticles *Algorithms* **2** 410–28
[18] Shao G, Shangguan Y, Tao J, Zheng J, Liu T and Wen Y 2018 An improved genetic algorithm for structural optimization of Au–Ag bimetallic nanoparticles *Appl. Soft Comput. J.* **73** 39–49
[19] Yun K, Cho Y-H, Cha P-R, Lee J, Nam H-S, Oh J S, Choi J-H and Lee S-C 2012 Monte Carlo simulations of the structure of Pt-based bimetallic nanoparticles *Acta Mater.* **60** 4908–16
[20] Wang B, Liu M, Wang Y and Chen X 2011 Structures and energetics of silver and gold nanoparticles *J. Phys. Chem.* C **115** 11374–81
[21] Jones J E 1924 On the determination of molecular fields.—II. From the equation of state of a gas *Proc. R. Soc.* A **106** 709–18
[22] Morse P M 1929 Diatomic molecules according to the wave mechanics. II. Vibrational levels *Phys. Rev.* **34** 57–64
[23] Daw M S and Baskes M I 1984 Embedded-atom method: derivation and application to impurities, surfaces, and other defects in metals *Phys. Rev.* B **29** 6443–53
[24] Finnis M W and Sinclair J E 1984 A simple empirical N-body potential for transition metals *Phil. Mag.* A **50** 45–55
[25] Baskes M I 1992 Modified embedded-atom potentials for cubic materials and impurities *Phys. Rev.* B **46** 2727–42
[26] Pishkenari H N, Yousefi F S and Taghibakhshi A 2019 Determination of surface properties and elastic constants of FCC metals: a comparison among different EAM potentials in thin film and bulk scale *Mater. Res. Express* **6** 015020
[27] Etesami S A and Asadi E 2018 Molecular dynamics for near melting temperatures simulations of metals using modified embedded-atom method *J. Phys. Chem. Solids* **112** 61–72
[28] Asadi E, Zaeem M A, Moitra A and Tschopp M A 2014 Effect of vacancy defects on generalized stacking fault energy of fcc metals *J. Phys.: Condens. Matter* **26** 115404
[29] Müller M and Albe K 2007 Concentration of thermal vacancies in metallic nanoparticles *Acta Mater.* **55** 3237–44
[30] Lee B-J and Baskes M I 2000 Second nearest-neighbor modified embedded-atom-method potential *Phys. Rev.* B **62** 8564–7
[31] Lee B-J, Shim J-H and Baskes M I 2003 Semiempirical atomic potentials for the fcc metals Cu, Ag, Au Ni, Pd, Al and Pb based on first and second nearest-neighbor modified embedded atom method *Phys. Rev.* B **68** 144112
[32] Hofmeister H, Tan G L and Dubiel M 2005 Shape and internal structure of silver nanoparticles embedded in glass *J. Mater. Res.* **20** 1551–62
[33] Khan M A M, Kumar S, Ahamed M, Alrokayan S A and AlSalhi M S 2011 Structural and thermal studies of silver nanoparticles and electrical transport study of their thin films *Nanoscale Res. Lett.* **6** 434
[34] Martínez Espinosa J C, Carrera Cerritos R, Ramírez Morales M A, Sánchez Guerrero K P, Silva Contreras R A

and Macías J H 2020 Characterization of silver nanoparticles obtained by a green route and their evaluation in the bacterium of pseudomonas aeruginosa *Crystals* **10** 395
[35] Lu Y, Mei Y, Schrinner M, Ballauff M, Möller M and Breu J 2007 *In situ* formation of Ag nanoparticles in spherical polyacrylic acid brushes by UV irradiation *J. Phys. Chem.* C **111** 7676–81
[36] Pyatenko A, Yamaguchi M and Suzuki M 2007 Synthesis of spherical silver nanoparticles with controllable sizes in aqueous solutions *J. Phys. Chem.* C **111** 7910–7
[37] Torras M and Roig A 2020 From silver plates to spherical nanoparticles: snapshots of microwave-assisted synthesis *ACS Omega* **5** 5731–8
[38] Kraftmakher Y 1998 Equilibrium vacancies and thermophysical properties of metals *Phys. Rep.* **299** 79–188
[39] Guedj C, Barnes J P and Papon A M 2006 Atomic scale observation of corner-voiding effects in advanced interconnects *Appl. Phys. Lett.* **89** 203108
[40] Gilbert M R, Yao Z, Kirk M A, Jenkins M L and Dudarev S L 2009 Vacancy defects in Fe: comparison between simulation and experiment *J. Nucl. Mater.* **386–388** 36–40
[41] Sharma S K, Sudarshan K, Maheshwari P, Dutta D, Pujari P K, Shah C P, Kumar M and Bajaj P 2011 Direct evidence of Cd vacancies in CdSe nanoparticles: positron annihilation studies *Eur. Phys. J.* B **82** 335–40
[42] Proffen T and Neder R B 1997 DISCUS: a program for diffuse scattering and defect-structure simulation *J. Appl. Crystallogr.* **30** 171–5
[43] Cervellino A, Giannini C and Guagliardi A 2010 DEBUSSY: a Debye user system for nanocrystalline materials *J. Appl. Crystallogr.* **43** 1543–7
[44] Beyerlein K R, Leoni M, Snyder R L, Li M and Scardi P 2010 Simulating the temperature effect in a powder diffraction pattern with molecular dynamics *European Powder Diffraction Conf.* (Darmstadt: Oldenbourg Wissenschaftsverlag) (https://doi.org/10.1524/9783486991321-011)
[45] Beyerlein K, Cervellino A, Leoni M, Snyder R L and Scardi P 2015 Debye equation versus whole powder pattern modelling: real versus reciprocal space modelling of nanomaterials *Eleventh European Powder Diffraction Conf.* (Darmstadt: Oldenbourg Wissenschaftsverlag) (https://doi.org/10.1524/9783486992588-017)
[46] Scardi P and Leoni M 2004 Whole powder pattern modelling: theory and applications *Diffraction Analysis of the Microstructure of Materials* (Berlin: Springer) (https://doi.org/10.1007/978-3-662-06723-9_3)
[47] Gelisio L and Scardi P 2016 100 years of Debye's scattering equation *Acta Cryst.* A **72** 608–20
[48] Macrae C F, Edgington P R, McCabe P, Pidcock E, Shields G P, Taylor R, Towler M and van de Streek J 2006 Mercury: visualization and analysis of crystal structures *J. Appl. Crystallogr.* **39** 453–7
[49] Somorjai G A and McCrea K 2001 Roadmap for catalysis science in the 21st century: a personal view of building the future on past and present accomplishments *Appl. Catal. A: Gen.* **222** 3–18
[50] Taylor H S 1925 A theory of the catalytic surface *Proc. R. Soc.* A **108** 105–11
[51] Stenlid J H and Brinck T 2017 Extending the σ-hole concept to metals: an electrostatic interpretation of the effects of nanostructure in gold and platinum catalysis *J. Am. Chem. Soc.* **139** 11012–5
[52] Casas-Cabanas M, Binotto G, Larcher D, Lecup A, Giordani V and Tarascon J-M 2009 Defect chemistry and catalytic activity of nanosized Co_3O_4 *Chem. Mater.* **21** 1939–47
[53] Kim D, Chung M, Kim S, Yun K, Cha W, Harder R and Kim H 2019 Defect dynamics at a single Pt nanoparticle during catalytic oxidation *Nano Lett.* **19** 5044–52
[54] Jia Y, Jiang K, Wang H and Yao X 2019 The role of defect sites in nanomaterials for electrocatalytic energy conversion *Chem* **5** 1371–97
[55] Chattot R *et al* 2018 Surface distortion as a unifying concept and descriptor in oxygen reduction reaction electrocatalysis *Nat. Mater.* **17** 827–33
[56] Stöber W, Fink A and Bohn E 1968 Controlled growth of monodisperse silica spheres in the micron size range *J. Colloid Interface Sci.* **26** 62–69
[57] Jurkiewicz K, Kamiński M, Glajcar W, Woźnica N, Julienne F, Bartczak P, Polański J, Lelątko J, Zubko M and Burian A 2018 Paracrystalline structure of gold, silver, palladium and platinum nanoparticles *J. Appl. Crystallogr.* **51** 411–9
[58] Billinge S J and Kanatzidis M G 2004 Beyond crystallography: the study of disorder, nanocrystallinity and crystallographically challenged materials with pair distribution functions *Chem. Comm.* 749–60
[59] Billinge S J L and Levin I 2007 The problem with determining atomic structure at the nanoscale *Science* **316** 561–5
[60] Billinge S J L 2019 The rise of the x-ray atomic pair distribution function method: a series of fortunate events *Phil. Trans. R. Soc.* A **377** 20180413
[61] Thompson A P *et al* 2022 LAMMPS-A flexible simulation tool for particle-based materials modeling at the atomic, meso, and continuum scales *Comput. Phys. Commun.* **271** 108171
[62] Suh I-K, Ohta H and Waseda Y 1988 High-temperature thermal expansion of six metallic elements measured by dilatation method and x-ray diffraction *J. Mater. Sci.* **23** 757–60
[63] Kamiński M, Jurkiewicz K, Burian A and Bródka A 2020 The structure of gold nanoparticles: molecular dynamics modeling and its verification by x-ray diffraction *J. Appl. Crystallogr.* **53** 1–8
[64] Egami T and Billinge S J 2003 *Underneath the Bragg Peaks: Structural Analysis of Complex Materials* (Amsterdam: Elsevier)
[65] Menke H 1932 Rontgeninterferenzen an Flüssigkeiten (Hg, Ga, CCl_4) *Phys. Z.* **33** 593–604
[66] Bates S 2019 X-ray diffraction from non-crystalline materials: the Debye model *International Tables for Crystallography* vol H (New York: Wiley) ch 5.6, pp 617–48
[67] Mitchell G R 1981 Eliminating the small-angle component of the scattering calculated for models *Acta Cryst.* A **37** 488–90
[68] Klug H P and Alexander L E 1974 *X-ray Diffraction Procedures for Polycrystalline and Amorphous Materials* 2nd edn (New York: Wiley)
[69] Hosemann R and Bagchi S N 1962 *Direct Analysis of Diffraction by Matter* (Amsterdam: North-Holland Publishing Company)
[70] Toby B H 2006 R factor in Rietveld analysis: how good is good enough *Powder Diffr.* **21** 67–70
[71] Purwaningroom D L and Arifin R 2017 Performance of EAM and MEAM potential for NiTi alloys *IOP Conf. Ser.: Mater. Sci. Eng.* **180** 012252
[72] Cherne F J, Baskes M I and Deymier P A 2001 Properties of liquid nickel: a critical comparison of EAM and MEAM calculations *Phys. Rev.* B **65** 024209
[73] Kanhaiya K, Kim S, Im W and Heinz H 2021 Accurate simulation of surfaces and interfaces of ten FCC metals and steel using Lennard–Jones potentials *npj Comput. Mater.* **7** 17

[74] Xiong S, Lee S-Y and Noyan I C 2019 Average and local strain fields in nanocrystals *J. Appl. Crystallogr.* **52** 262–73
[75] Padilla Espinosa I M, Jacobs T D B and Martini A 2021 Evaluation of force fields for molecular dynamics simulations of platinum in bulk and nanoparticle forms *J. Chem. Theory Comput.* **17** 4486–98
[76] Chen S, Aitken Z H, Sorkin V, Yu Z G, Wu Z and Zhang Y-W 2022 Modified embedded-atom method potentials for the plasticity and fracture behaviors of unary HCP metals *Adv. Theory Simul.* **5** 2100377
[77] Moskovkin P and Hou M 2007 Metropolis Monte Carlo predictions of free Co–Pt nanoclusters *J. Alloys Compd.* **435** 550–4
[78] Loffreda D, Foster D M, Palmer R E and Tarrat N 2021 Importance of defective and nonsymmetric structures in silver nanoparticles *J. Phys. Chem. Lett.* **12** 3705–11
[79] Guisbiers G 2011 Schottky defects in nanoparticles *J. Phys. Chem.* C **115** 2616–21
[80] Borisyuk P V, Pushkin M A, Tronin I V, Troyan V I and Vasiliev O S 2012 Vacancy mechanism of melting and surface roughening of metal nanoparticles *Int. J. Mod. Phys.* B **26** 1250167
[81] Salis M, Carbonaro C M, Marceddu M and Ricci P C 2013 Statistical thermodynamics of schottky defects in metal nanoparticles *Nanosci. Nanotechnol.* **3** 27–33
[82] Gao P, Ma H, Wu Q, Qiao L, Volinsky A A and Su Y 2016 Size-dependent vacancy concentration in nickel, copper, gold, and platinum nanoparticles *J. Phys. Chem.* C **120** 17613–9
[83] Qi W H and Wang M P 2004 Vacancy formation energy of small particles *J. Mater. Sci.* **39** 2529–30
[84] Kaatz F H, Bultheel A and Ori O 2017 Kinetic Monte Carlo approach to Schottky defects in noble metal nanoclusters *J. Math. Chem.* **55** 34–49
[85] Cimino A, Porta P and Valigi M 1966 Dependence of the lattice parameter of magnesium oxide on crystallite size *J. Am. Ceram. Soc.* **49** 152–6
[86] Ayyub P, Palkar V, Chattopadhyay S and Multani M 1995 Effect of crystal size reduction on lattice symmetry and cooperative properties *Phys. Rev.* B **51** 6135–8
[87] Tsunekawa S, Ito S, Mori T, Ishikawa K, Li Z-Q and Kawazoe Y 2000 Critical size and anomalous lattice expansion in nanocrystalline $BaTiO_3$ particles *Phys. Rev.* B **62** 3065–70
[88] Ahmad M I and Bhattacharya S S 2009 Size effect on the lattice parameters of nanocrystalline anatase *Appl. Phys. Lett.* **95** 191906
[89] Prieur D *et al* 2020 Size dependence of lattice parameter and electronic structure in CeO_2 nanoparticles *Inorg. Chem.* **59** 5760–7
[90] Wasserman H J and Vermaak J S 1970 On the determination of a lattice contraction in very small silver particles *Surf. Sci.* **22** 164–72
[91] Sheng J, Welzel U and Mittemeijer E J 2010 Nonmonotonic crystallite-size dependence of the lattice parameter of nanocrystalline nickel *Appl. Phys. Lett.* **97** 153109
[92] Ohshima K and Harada J 1984 An x-ray diffraction study of soft surface vibrations of fcc fine metal particles *J. Phys. C: Solid State Phys.* **17** 1607–16
[93] Onodera S 1992 Lattice parameters of fine copper and silver particles *J. Phys. Soc. Japan* **61** 2190–3
[94] Dubiel M, Brunsch S, Seifert W, Hofmeister H and Tan G L 2001 Stress state of silver nanoparticles embedded in a silicate glass matrix investigated by HREM and EXAFS spectroscopy *Eur. Phys. J.* D **8** 229–32
[95] Zhang Q, Li W, Moran C, Zeng J, Chen J, Wen L-P and Xia Y 2010 Seed-mediated synthesis of Ag nanocubes with controllable edge lengths in the range of 30–200 nm and comparison of their optical properties *J. Am. Chem. Soc.* **132** 11372–8
[96] Mukherji S, Bharti S, Shukla G and Mukherji S 2019 Synthesis and characterization of size-and shape-controlled silver nanoparticles *Phys. Science Rev.* **4** 20170082
[97] Qi W H and Wang M P 2005 Size and shape dependent lattice parameters of metallic nanoparticles *J. Nanopart. Res.* **7** 51–57
[98] Lei Y *et al* 2014 Adsorbate-induced structural changes in 1–3 nm platinum nanoparticles *J. Am. Chem. Soc.* **136** 9320–6
[99] Harada M, Ikegami R, Kumara L S R, Kohara S and Sakata O 2019 Reverse Monte Carlo modeling for local structures of noble metal nanoparticles using high-energy XRD and EXAFS *RSC Adv.* **9** 29511–21
[100] Taherkhani F, Negreiros F R, Parsafar G and Fortunelli A 2010 Simulation of vacancy diffusion in a silver nanocluster *Chem. Phys. Lett.* **498** 312–6
[101] Hosemann R, Hentschel M P, Balta-Calleja F J and Yeh G S Y 1983 Generalisation of PP Ewald's intensity function for microparacrystals in colloids and their superstructures *J. Phys. C: Solid State Phys.* **16** 4959–71
[102] Ryu U, Jee S, Rao P C, Shin J, Ko C, Yoon M, Park K S and Choi K M 2021 Recent advances in process engineering and upcoming applications of metal–organic frameworks *Coord. Chem. Rev.* **426** 213544
[103] Chistyakova N and Tran T M H 2016 A study of the applicability of different types of interatomic potentials to compute elastic properties of metals with molecular dynamics methods *AIP Conf. Proc.* **1772** 060019
[104] Chen T and Manz T A 2019 A collection of forcefield precursors for metal–organic frameworks *RSC Adv.* **9** 36492–507
[105] Sneed B T, Young A P and Tsung C-K 2015 Building up strain in colloidal metal nanoparticle catalysts *Nanoscale* **7** 12248–65